The Astrophysical Journal Letters, 954:L7 (11pp), 2023 September 1 https://doi.org/10.3847/2041-8213/acefb5

The FRB 20190520B Sight Line Intersects Foreground Galaxy Clusters

Khee-Gan Lee[1,2], Ilya S. Khrykin[1,2], Sunil Simha[3], Metin Ata[4], Yuxin Huang[1], J. Xavier Prochaska[1,3,5], Nicolas Tejos[6], Jeff Cooke[7,8,9], Kentaro Nagamine[1,10,11], and Jielai Zhang[7,8]
[1] Kavli IPMU (WPI), UTIAS, The University of Tokyo, Kashiwa, Chiba 277-8583, Japan; kglee@ipmu.jp
[2] Center for Data-Driven Discovery, Kavli IPMU (WPI), UTIAS, The University of Tokyo, Kashiwa, Chiba 277-8583, Japan
[3] University of California–Santa Cruz, 1156 High St., Santa Cruz, CA 95064, USA
[4] The Oskar Klein Centre, Department of Physics, Stockholm University, AlbaNova University Centre, SE-106 91 Stockholm, Sweden
[5] Division of Science, National Astronomical Observatory of Japan, 2-21-1 Osawa, Mitaka, Tokyo 181-8588, Japan
[6] Instituto de Física, Pontificia Universidad Católica de Valparaíso, Casilla 4059, Valparaíso, Chile
[7] Centre for Astrophysics and Supercomputing, Swinburne University of Technology, Hawthorn, VIC, 3122, Australia
[8] Australian Research Council Centre of Excellence for Gravitational Wave Discovery (OzGrav), Australia
[9] Australian Research Council Centre of Excellence for All-Sky Astrophysics in 3 Dimensions (ASTRO-3D), Australia
[10] Department of Earth and Space Science, Graduate School of Science, Osaka University, Toyonaka, Osaka, 560-0043, Japan
[11] Department of Physics & Astronomy, University of Nevada Las Vegas, Las Vegas, NV 89154, USA
Received 2023 June 9; revised 2023 August 8; accepted 2023 August 10; published 2023 August 25

Abstract

The repeating fast radio burst FRB 20190520B is an anomaly of the FRB population thanks to its high dispersion measure (DM = 1205 pc cm^{-3}) despite its low redshift of $z_{\rm frb} = 0.241$. This excess has been attributed to a large host contribution of $\rm DM_{host} \approx 900\,pc\,cm^{-3}$, far larger than any other known FRB. In this paper, we describe spectroscopic observations of the FRB 20190520B field obtained as part of the FLIMFLAM survey, which yielded 701 galaxy redshifts in the field. We find multiple foreground galaxy groups and clusters, for which we then estimated halo masses by comparing their richness with numerical simulations. We discover two separate $M_{\rm halo} > 10^{14}\,M_{\odot}$ galaxy clusters at $z = 0.1867$ and 0.2170 that are directly intersected by the FRB sight line within their characteristic halo radius r_{200}. Subtracting off their estimated DM contributions, as well that of the diffuse intergalactic medium, we estimate a host contribution of $\rm DM_{host} = 430^{+140}_{-220}$ or 280^{+140}_{-170} pc cm^{-3} (observed frame), depending on whether we assume that the halo gas extends to r_{200} or $2 \times r_{200}$. This significantly smaller $\rm DM_{host}$—no longer the largest known value—is now consistent with Hα emission measures of the host galaxy without invoking unusually high gas temperatures. Combined with the observed FRB scattering timescale, we estimate the turbulent fluctuation and geometric amplification factor of the scattering layer to be $\widetilde{F}G \approx 4.5$–$11\,(\rm pc^2\,km)^{-1/3}$, suggesting that most of the gas is close to the FRB host. This result illustrates the importance of incorporating foreground data for FRB analyses both for understanding the nature of FRBs and to realize their potential as a cosmological probe.

Unified Astronomy Thesaurus concepts: Radio transient sources (2008); Intergalactic gas (812); Circumgalactic medium (1879); Redshift surveys (1378)

Supporting material: data behind figure, interactive figures

1. Introduction

Fast radio bursts (FRBs) are phenomena that have excited tremendous interest, not just because of the enigmatic nature of their source engines but also because their frequency sweeps encode information on the integrated free electron column density along their lines of sight. This is usually quantified through the dispersion measure, $\rm DM = \int n_e(l)\,dl$, where $n_e(l)$ is the free electron density along the line-of-sight path l.

Among the sample of FRBs that have been localized at the time of writing, FRB 20190520B ranks among the most notable. First reported by Niu et al. (2022), it was discovered as a sequence of repeating bursts by the Five-Hundred Aperture Spherical Radio Telescope (Nan et al. 2011; Li et al. 2018) that was subsequently localized with the Karl G. Jansky Very Large Array (Law et al. 2018) to the equatorial J2000 coordinates (R.A., decl.) = (16:02:04.261, −11:17:17.35). Follow-up optical imaging and spectroscopy revealed a host galaxy, J160204.31−111718.5 (hereafter referred to as 59 HG190520), that was associated with the FRB at high confidence. This galaxy was measured to have a spectroscopic redshift of $z_{\rm frb} = 0.241$ and also has an associated persistent radio source.

With a total measured DM of $\rm DM_{FRB} = 1204.7 \pm 4.0\,pc\,cm^{-3}$ (Niu et al. 2022), FRB 20190520B has a DM well in excess of the value expected given its redshift and Macquart relation (Macquart et al. 2020); assuming a Milky Way contribution of $\rm DM_{MW} \sim 100\,pc\,cm^{-3}$ and a mean intergalactic medium (IGM) contribution of $\langle \rm DM_{IGM} \rangle \sim 300\,pc\,cm^{-3}$ (using the rough approximations of Ioka 2003 and Inoue 2004), FRB 20190520B exhibits a DM over twice that expected given its redshift. This was attributed to a large host contribution of $\rm DM_{host} = 903^{+72}_{-111}$ pc cm^{-3} (observed frame; Niu et al. 2022), which makes it by far the largest host DM value of any known FRB prior to the current analysis.

While Niu et al. (2022) and Ocker et al. (2022) concluded that no foreground galaxies were likely to contribute to the foreground DM, they based this conclusion on a single pointing of Keck/LRIS observations that was limited to ∼2′–3′ from the FRB sight line. This would be adequate to reveal, for example,

the influence of a foreground galaxy at $z = 0.15$ with a halo mass of $M_{\rm halo} \sim 10^{12}\,M_{\odot}$, since its characteristic radius of $r_{200} \approx 240$ pkpc would extend 1.′5. However, a modestly more massive foreground halo with, say, $M_{\rm halo} \sim 3 \times 10^{13}\,M_{\odot}$ at the same redshift would have an r_{200} extending to 4.′7 from the halo center. This would be outside the field of the original optical observations and require wide field-of-view multiplexed spectroscopy to characterize the multiple member galaxies. Wider observations than originally achieved in the discovery papers are therefore needed to rule out significant foreground contributions to the large DM of FRB 20190520B.

In this paper, we describe the wide-field multiplexed spectroscopic data we have obtained in the FRB 20190520B field as part of the FRB Line-of-sight Ionization Measurement From Lightcone AAOmega Mapping (FLIMFLAM) survey (Lee et al. 2022). This survey, which is carried out on the 2dF/AAOmega fiber spectrograph on the 3.9 m Anglo-Australian Telescope (AAT) in Siding Spring, Australia, is designed to observed large numbers of galaxy redshifts in the foregrounds of localized FRBs in order to map the large-scale structure in the foreground. As shown by Simha et al. (2020), this would allow us to separate the various components that make up the DM observed in FRBs. We then describe the group-finding approach applied to the spectroscopic data using a commonly used friends-of-friends (FoF) algorithm to identify galaxy groups and clusters within the FRB 20190520B field. The group/cluster halo masses are then estimated by comparing with forward models of group/cluster richness derived from cosmological *N*-body simulations. Next, we model the implied DM from both the foreground halos and diffuse IGM, yielding updated estimates for the FRB 20190520B DM host contribution. Finally, we discuss the implications of the new host estimate in the context of the observed host galaxy Hα emission and FRB scattering. In a separate paper, Simha et al. (2023) analyzed four other sight lines also shown to exhibit an excess $\rm DM_{FRB}$ given their redshift, but FRB 20190520B was deemed such an unusual object that it merited a separate analysis and paper.

In this paper, we use the term "groups" to refer to both groups and clusters when we are agnostic as to their underlying halo masses but "cluster" to refer specifically to objects with $M_{\rm halo} \geqslant 10^{14}\,M_{\odot}$. We use a concordance ΛCDM cosmology with $\sigma_8 = 0.829$, $H_0 = 67.3\,{\rm km\,s^{-1}\ Mpc^{-1}}$, $h = H_0/(100\,{\rm km\,s^{-1}\ Mpc^{-1}}) = 0.673$, $\Omega_\Lambda = 0.685$, $\Omega_m = 0.315$, $\Omega_b = 0.0487$, and $n = 0.96$.

2. Observations

In order to characterize the foreground contributions to the FRB 20190520B DM, we carried out a sequence of observations as part of the broader FLIMFLAM survey (Lee et al. 2022). Since FRB 20190520B was immediately reported to have an anomalously high $\rm DM_{host}$ by Niu et al. (2022), it was deemed to be of sufficient scientific interest to constrain the foreground contributions of FRB 20190520B; therefore, it was added to the FLIMFLAM observation list as a special target.

To our knowledge, FRB 20190520B was not within the footprint of publicly available imaging surveys; therefore, on 2021 August 8, we imaged the field with a single pointing of the Dark Energy Camera (DECam) in the *r* band. The data were then reduced using the standard pipeline provided by the observatory and a galaxy catalog generated using `SExtractor` (Bertin & Arnouts 1996) after excluding point sources as stars. Since the DECam imaging preceded the spectroscopic run with AAT/AAOmega by only 1 month, at the time of spectroscopic target selection, we had only preliminary image reductions that did not have a well-characterized magnitude zero-point. For the spectroscopic target selection, we therefore defined an arbitrary magnitude cut in the *r* band to select approximately 1500 targets within the 2° diameter (i.e., 3.14 $\rm deg^2$) footprint of AAT/AAOmega. This was intended to target an areal density of galaxies that should, on average, correspond approximately to a magnitude limit of $r \approx 19.4$ mag, which is our magnitude limit for FRBs at $z \approx 0.2$ (see Simha et al. 2023). However, this selection was later found to actually correspond to an apparent depth of $r = 19.1$ mag or unextincted magnitude of $r_{\rm dered} = 18.4$ mag based on corrections using the Schlafly & Finkbeiner (2011) dust map.[12] This field is thus overdense in galaxies given the relative shallowness of the magnitude threshold, as we shall see later. We note that there is significant variation (∼0.4 mag) in the extinction across our 3.1 $\rm deg^2$ field, which makes it challenging to compare the number counts with simulations, but our forward model described later should be accurate in the vicinity of the FRB position.

Using `configure` (Miszalski et al. 2006), the standard plate configuration software provided by the observatory, we designed five plates filled with approximately 300 galaxies, each across the 3.1 $\rm deg^2$ 2dF footprint, of which three were observed with AAOmega on UT 2021 September 7–9. The observing setup was the 580V grating blazed at 485 nm on the blue camera, while the red camera used the 385R grating blazed at 720 nm. In combination with the 570 nm dichroic, this allowed continuous spectral coverage across 380–880 nm with a spectral resolving power of $R \approx 1300$. Each plate received 4500–5400 s of on-sky exposure; the first plate was observed in suboptimal seeing of 3″–3.″5 on 2021 September 7, but the subsequent two plates were observed under nominal conditions in the following nights with 1.″6–1.″8 seeing.

The raw data were reduced using a version of the `2dFDR` data reduction package kindly provided by the OzDES collaboration (Yuan et al. 2015; Childress et al. 2017). We then ran the `MARZ` software (Hinton et al. 2016) on the spectra to measure spectroscopic redshifts, which were then visually confirmed. Redshift identifications that appeared to be a reasonable match to the spectral templates were assigned a quality operator (QOP) flag of 3, while high-confidence redshifts with multiple high signal-to-noise features were assigned QOP = 4. There were 701 galaxies that had QOP = (3 ∨ 4), which we consider to be "successful" redshifts and will treat identically in the subsequent analysis. The galaxy redshift histogram is shown in Figure 1, which shows distinct redshift peaks that are suggestive of overdensities within the field. This motivates us to apply group-finding algorithms to search for galaxy groups or clusters within the sample.

During visual inspection of the spectra, we found 122 confirmed stars compared to 701 galaxies, or a stellar contamination rate of 17.4%. This is relatively high compared to the other fields observed by FLIMFLAM, presumably due to the low Galactic latitude ($b = 29°$) and imperfect star–galaxy separation. If we assume that the stellar contamination rate is the same between the spectroscopically confirmed targets and those that could not be assigned a conclusive redshift, then the spectroscopic completeness success rate of our galaxy sample is 701 out of 1260 possible galaxy targets, or 56.6%.

[12] For notational clarity, all magnitudes subsequently quoted in this paper will implicitly be corrected for dust extinction magnitudes unless stated otherwise.

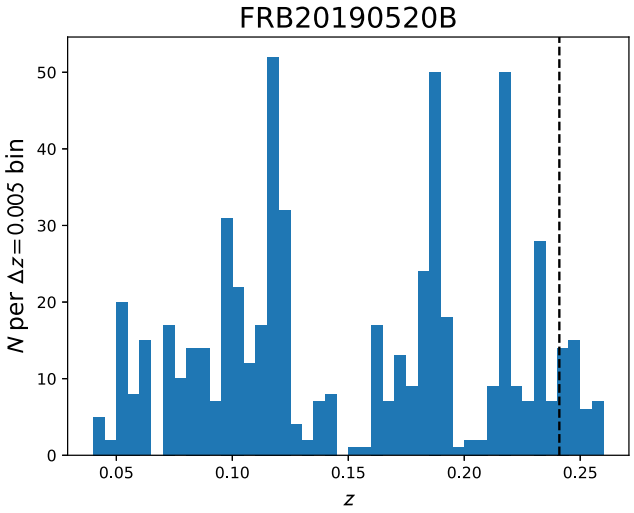

Figure 1. Galaxy redshift distribution from our AAT/2dF-AAOmega spectroscopic observations, which targeted an approximately 2° field of view centered on FRB 20190520B. The FRB redshift ($z_{\rm frb} = 0.241$) is indicated by the vertical dashed line.

3. Halos

We applied an anisotropic FoF group-finding algorithm on our FRB 20190520B spectroscopic data, kindly provided by Elmo Tempel (Tago et al. 2008; Tempel et al. 2012, 2014). While standard FoF algorithms, such as those used to identify dark matter halos in *N*-body simulations, typically adopt the same linking length in all three dimensions, Tempel's code allows for a longer linking length in the radial dimension in order to account for redshift space distortions, i.e., the "Fingers of God."

This finder assumes a transverse linking length, $d_{\rm LL,\perp}$, which varies as a function of redshift, z, in the following way:

$$d_{\rm LL,\perp}(z) = d_{\rm LL,0}[1 + a\ \arctan(z/z_*)], \quad (1)$$

where $d_{\rm LL,0}$ is the linking length at a fiducial redshift, and a and z_* govern the redshift evolution. This redshift dependence accounts for the artificially decreasing number of galaxies as a function of redshift within a flux-limited survey. We then set the radial linking length, $d_{\rm LL,\parallel}(z)$, to be proportional to $d_{\rm LL,\perp}(z)$. The final parameters used for group-finding in this paper are $d_{\rm LL,\perp} = 0.35\,h^{-1}$ Mpc, $a = 0.75$, $z_* = 0.1$, and $d_{\rm LL,\parallel}/d_{\rm LL,\perp} = 10$. Note that we adopt a linking length that is larger than that used in Simha et al. (2023) in order to account for our sparser sample of redshifts, which is a nearly a factor of 2 lower space density than in Simha et al. (2023).

The resulting group catalog has groups with richness or multiplicity (i.e., number of identified galaxies) as low as $N_{\rm rich} = 2$, but we limit ourselves to $N_{\rm rich} = 4$ to have a more robust sample.[13] These are listed in Table 1, although note that we omit groups with $z_{\rm grp} > z_{\rm frb}$. We do not find any group with $z_{\rm grp} \approx z_{\rm frb}$ that can be plausibly associated with the FRB host.

In Figure 2, we present an interactive plot[14] that shows the position of the galaxies, as well as identified groups within the FRB field.

3.1. Estimating Group/Cluster Masses

In Simha et al. (2023), we adopted dynamical halo masses estimated using the virial theorem applied to the projected size and velocity dispersion of the galaxy groups. For the foreground sample of FRB 20190520B, however, the observations were much shallower, and the spectroscopic success rate was considerably lower than the equivalent data sets in Simha et al. (2023). For example, Simha et al. (2023) had 1493 galaxy redshifts for the FRB 20190714A field, which is at $z_{\rm frb} = 0.2365$, whereas for FRB 20190520B at a similar redshift of $z_{\rm frb} = 0.241$, we only have 701 successful galaxy redshifts. We therefore consider the FRB 20190520B sample too sparse for reliable application of the virial theorem for group/cluster mass estimation.

Instead, we use the group richness, $N_{\rm rich}$, combined with a forward-modeling approach based on semianalytic models of galaxy formation. Specifically, we use the Henriques et al. (2015) light-cone catalogs that were generated by applying the "Munich" semianalytic galaxy formation model (Guo et al. 2011) to the $L = 500\,h^{-1}$ Mpc Millennium *N*-body simulation (Springel 2005). In particular, we use the "all-sky" catalogs that are designed to simulate footprints covering 4π sr in order to maximize the number of simulated groups and clusters. We queried the simulation SQL database[15] to download $z < 0.25$ cluster catalogs with $\log_{10}(M_{\rm halo}/M_\odot) \geqslant 14.2$ from over the full sky, whereas for the halo mass range $13.0 \leqslant \log_{10}(M_{\rm halo}/M_\odot) < 14.2$, a subsample over a footprint of 400 deg^2 was deemed to provide a sufficient sample size to probe the diversity of the groups without having to download an excessively large file. This simulated group catalog includes effects such as *k*-corrected photometry based on the realistic galaxy spectral energy distributions (including the effect of dust), redshift space distortions, and the distance modulus (i.e., increasingly faint magnitudes as a function of redshift).

Using these mock catalogs, we build forward models matched to the observed redshift, $z_{\rm grp}$, of each detected group in our sample. First, we selected groups/clusters from the mock catalog within $z_{\rm grp} \pm 0.005$ and applied the same magnitude cut as that corresponding to our field center, $r \leqslant 18.42$ (with a small distance modulus correction to account for the finite width of the $\Delta z = 0.005$ redshift selection bin). This step yields $N_{\rm rich}^{\rm true}$ group members that would be observed within our observing setup if we had achieved 100% spectroscopic completeness. We then downsample each group to our actual observed completeness by drawing a random Poisson variate with a mean of $\mu = f_{\rm obs}\,N_{\rm rich}^{\rm true}$, where $f_{\rm obs} = 56.6\%$ is the completeness of our FRB 20190520B spectroscopy. The selected group galaxies are used to compute the observed mock richness, $N_{\rm rich}^{\rm mock} = \mu\,N_{\rm rich}^{\rm true}$, for that simulated group. In Figure 3, the gray lines show $N_{\rm rich}^{\rm mock}$ computed as a function of $\log_{10}(M_{\rm halo})$ for an ensemble of simulated groups selected to be at the same redshift as one of our observed groups. The scatter originates from both the intrinsic diversity of group properties at fixed halo mass and the stochasticity induced by the Poisson sampling at our low spectroscopic completeness. We then fit a spline function to obtain $N_{\rm rich}^{\rm mock}$ as a function of $\log_{10}(M_{\rm halo})$. While there are gaps in the sample of mock groups at certain masses, especially at the massive end, the spline fit appears to be a reasonable model for $N_{\rm rich}^{\rm mock}$ as a function of $\log_{10}(M_{\rm halo})$.

[13] We use a slightly more aggressive richness cut than in Simha et al. (2023) because we will not use the virial theorem to estimate mass.

[14] Made using Bokeh: http://www.bokeh.pydata.org.

[15] http://gavo.mpa-garching.mpg.de/MyMillennium

Table 1
Detected Galaxy Groups and Clusters in the FRB 20190520B Field

ID	z_{grp}	R.A.[a] (deg)	Decl.[a] (deg)	$b_\perp$[b] (arcmin)	$b_\perp$[b] (kpc)	N_{rich}[c]	$\log_{10}\left(\frac{M_{halo}}{M_\odot}\right)$	r_{200}[d] (kpc)	$b_\perp$[b] (r_{200})
2403390701118753	0.0536	240.3391	−11.1875	12.13	789.1	4	$12.87^{+0.21}_{-0.90}$	453	1.74
2400721001053090	0.0605	240.0721	−10.5309	52.48	3820.3	7	$13.33^{+0.10}_{-0.10}$	644	5.93
2407627701151079	0.0608	240.7628	−11.5108	19.65	1437.7	4	$12.94^{+0.28}_{-0.23}$	478	3.01
2402176201159096	0.0745	240.2176	−11.5910	25.33	2236.3	6	$13.35^{+0.15}_{-0.28}$	654	3.42
2399925001187499	0.0991	239.9925	−11.8750	46.83	5342.0	5	$13.41^{+0.16}_{-0.46}$	685	7.80
2404259001164001	0.1114	240.4259	−11.6400	21.79	2753.9	4	$13.20^{+0.34}_{-0.37}$	583	4.72
2404782701043103	0.1133	240.4783	−10.4310	51.48	6602.6	4	$13.38^{+0.23}_{-0.58}$	670	9.86
2401932701109639	0.1163	240.1933	−11.0964	22.30	2925.7	4	$13.41^{+0.25}_{-0.59}$	685	4.27
2395862301164344	0.1166	239.5862	−11.6434	58.78	7728.4	4	$13.39^{+0.25}_{-0.56}$	675	11.45
2404329301079377	0.1169	240.4329	−10.7938	30.08	3965.7	5	$13.52^{+0.19}_{-0.43}$	746	5.32
2405894601098030	0.1176	240.5895	−10.9803	18.95	2509.3	4	$13.46^{+0.21}_{-0.63}$	712	3.52
2406789301111492	0.1189	240.6789	−11.1149	14.07	1881.9	4	$13.46^{+0.21}_{-0.58}$	712	2.64
2409852201173268	0.1211	240.9852	−11.7327	38.30	5203.4	6	$13.67^{+0.17}_{-0.30}$	836	6.22
2408283601132797	0.1228	240.8284	−11.3280	18.43	2533.4	5	$13.58^{+0.20}_{-0.48}$	781	3.25
2408321001051411	0.1727	240.8321	−10.5141	50.00	9140.7	4	$13.95^{+0.23}_{-0.47}$	1037	8.81
2411417701121786	0.1741	241.1418	−11.2179	36.96	6803.0	5	$14.06^{+0.20}_{-0.30}$	1128	6.03
2402401701215090	0.1833	240.2402	−12.1509	54.27	10,409.6	4	$14.14^{+0.19}_{-0.83}$	1200	8.68
2405098001170259	0.1851	240.5098	−11.7026	24.87	4807.9	6	$14.31^{+0.19}_{-0.30}$	1367	3.52
2405265701133378	0.1867	240.5266	−11.3338	2.79	542.4	6	$14.34^{+0.18}_{-0.28}$	1399	0.39
2401408901101955	0.2164	240.1409	−11.0195	27.42	5989.1	5	$14.53^{+0.19}_{-0.31}$	1619	3.70
2406051301130845	0.2170	240.6051	−11.3084	5.28	1155.5	4	$14.44^{+0.20}_{-0.40}$	1511	0.76
2407679601092642	0.2175	240.7680	−10.9264	26.23	5750.6	7	$14.71^{+0.18}_{-0.25}$	1858	3.09
2405885701164888	0.2315	240.5886	−11.6489	22.04	5065.3	4	$14.58^{+0.22}_{-0.43}$	1682	3.01

Notes.
[a] R.A. and decl. in equatorial J2000 coordinates.
[b] Impact parameter from the FRB sight line in various units.
[c] Observed group richness.
[d] Halo characteristic radius at which matter density is 200× the critical density.

To estimate the halo masses, we then use the standard χ^2 minimization methodology,

$$\chi^2 = \frac{(N_{rich} - N_{rich}^{mock})^2}{\sigma_N^2}, \quad (2)$$

where $\sigma_N = \sqrt{N_{rich}}$ is the observational error on N_{rich}, which we estimate to be simply the Poisson uncertainty. We evaluate this on a grid of halo masses in the range $13.0 < \log_{10}(M_{halo}/M_\odot) < 14.9$ using the spline-fit model for N_{rich}^{mock} described above obtained for each redshift. The best-fit halo mass is given by the minimum χ^2, while we also estimate the 68th percentile uncertainties by evaluating the halo masses at $\Delta\chi^2 = 1$. The estimated halo masses are listed in Table 1, along with the corresponding r_{200}, the characteristic halo radius within which the halo matter density is 200× the mean density of the Universe at that redshift.

Notably, we find several foreground galaxy clusters with halo masses of $\log_{10}(M_{halo}/M_\odot) > 14$. Two of these clusters are intersected by the FRB sight line within their characteristic cluster radius: (1) at $z_{grp} = 0.1867$, a galaxy cluster with $\log_{10}(M_{halo}/M_\odot) = 14.34^{+0.18}_{-0.28}$ lies a mere 2.′79 or $b_\perp = 542$ pkpc from the FRB sight line, which corresponds to $0.388 \times r_{200}$, and (2) another, separate, cluster is at $z = 0.2170$ with an estimated halo mass of $\log_{10}(M_{halo}/M_\odot) = 14.44^{+0.20}_{-0.40}$, intersecting the sight line at $0.765 \times r_{200}$.

At first glance, it might appear that there are preferentially more low-mass groups at the low-redshift end of our spectroscopic data, while the more massive clusters lie preferentially toward the higher redshifts. However, this is a selection effect in that only more massive groups or clusters are detectable as multiple galaxy members with our relatively shallow magnitude threshold and low completeness. This is shown in Figure 4, in which we use the light-cone galaxy catalogs of Henriques et al. (2015) to derive the expected completeness of $N_{rich} \geqslant 4$ groups and clusters as a function of halo mass and redshift. This takes into account the estimated observational depth and incompleteness, as well as the intrinsic variance in the number of member galaxies for each halo mass. The masses that can be selected do indeed increase as a function of redshift, consistent with what we see in our data. While we are confident that we have ruled out massive clusters at $z < 0.15$ in our field, we suspect that more complete spectroscopic observations would reveal multiple lower-mass groups associated with the clusters detected at $z > 0.17$. Indeed, our detected clusters are not isolated, with multiple entities detected at similar redshifts —indicative of true overdensities and related structures in the cosmic web.

4. Analysis

In this paper, we adopt the observed DM value of $DM_{FRB} = (1205 \pm 4)$ pc cm^{-3} for FRB 20190520B, as reported by Niu et al. (2022). We then decompose the total

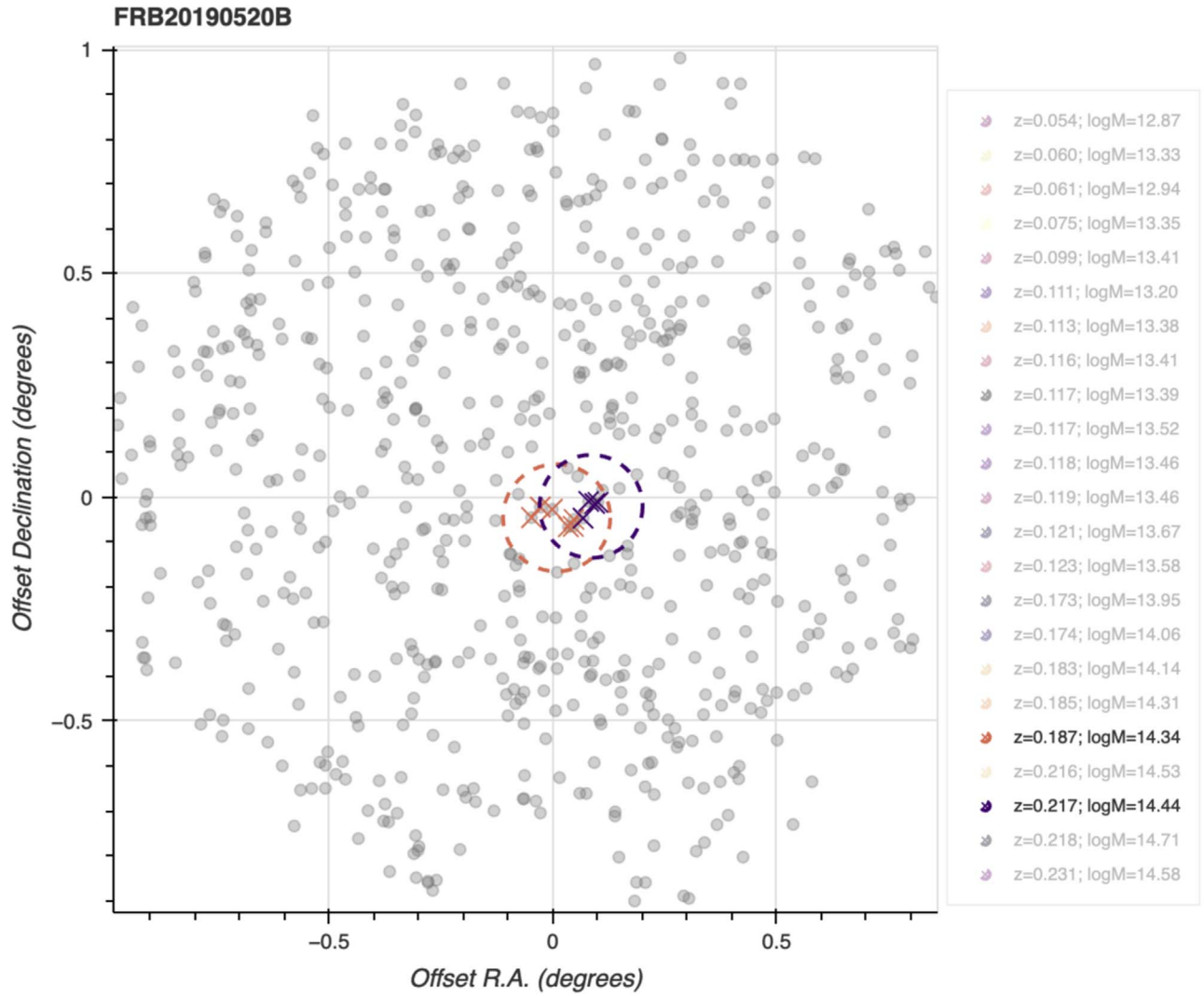

Figure 2. Preview of an interactive visualization of the FLIMFLAM foreground redshifts in the FRB 20190520B field (click on this URL for an external copy). The gray points indicate galaxies with measured spectroscopic redshifts, with their positions on the sky shown as a relative angular offset from the FRB 20190520B coordinate (i.e., the FRB is at [0, 0]). In the online version, pan dragging and zooming is supported (tool bar on top), while hovering over an individual galaxy with the mouse will show the coordinate and redshift. Clicking on the legend on the right will highlight galaxy groups labeled by redshift, with group members marked with crosses and the physical extent of r_{200} indicated by dashed circles. In the static preview, we have highlighted the clusters at $z_{\rm grp} = 0.1867$ and 0.2170 that are believed to provide large contributions to $\rm DM_{halos}$. The interactive figure is available in the online journal. The data behind this figure are included in machine-readable format with the .tar.gz package.

(The data used to create this figure are available.)

observed DM contribution for FRB 20190520B into several components:

$$\rm DM_{FRB} = DM_{MW} + DM_{halos} + DM_{IGM} + DM_{host}, \quad (3)$$

where $\rm DM_{MW}$ is the contribution from the Milky Way, $\rm DM_{halos}$ is the summed contribution from individual halos[16] that intersect the sight line, $\rm DM_{IGM}$ is the contribution from the diffuse IGM outside of halos, and $\rm DM_{host}$ is the combined contribution from the host galaxy and FRB engine. Note that the notation $\rm DM_{IGM}$ is sometimes used to refer to the sum of $\rm DM_{halos}$ and $\rm DM_{IGM}$ in the literature, but in this paper, we explicitly separate out the IGM and halo contributions. For the Milky Way component, we use the same estimate by Niu et al. (2022) of $\rm DM_{MW} =$ 113 pc cm^{-3} for the disk and halo contribution from the Milky Way. The disk contribution was estimated by averaging the NE2001 (Cordes & Lazio 2002) and YMW16 (Yao et al. 2017) disk models. The Galactic halo contribution, on the other hand, was estimated using models from Prochaska & Zheng (2019), Cook et al. (2023), and Ravi et al. (2023).

In the following subsections, we will assess the contributions of $\rm DM_{halos}$ and $\rm DM_{IGM}$ based on our observational data.

4.1. Foreground Halo Contributions

We have now established that the FRB 20190520B sight line directly intersects within $<1\ r_{200}$ of at least two galaxy clusters in the foreground. In order to calculate the $\rm DM_{halos}$ contribution, we need to make assumptions about the distribution of free electrons in the circumhalo medium of these halos.

[16] We use $\rm DM_{halo}$ to refer to individual halo contributions, while $\rm DM_{halos}$ (note plural in subscript) is the aggregate quantity from all halos.

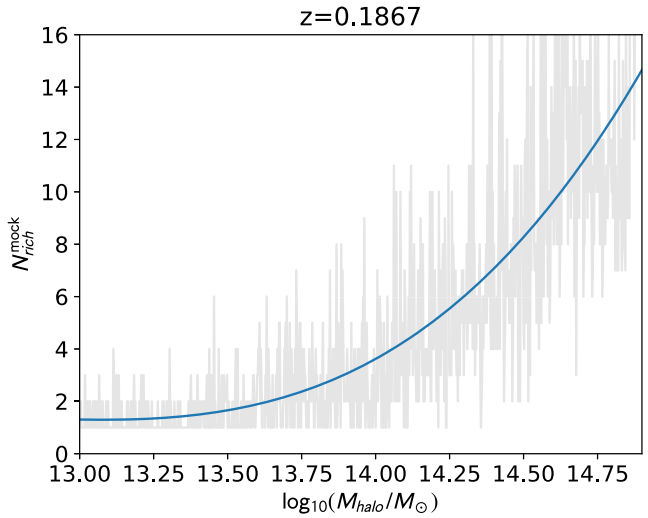

Figure 3. Example of our halo mass estimation model using the group richness, built from mock groups/clusters from the Millennium simulation. The gray lines show the richness of an ensemble of mock groups selected at the redshift of our detected group at $z_{grp} = 0.1867$ after incorporating the incompleteness and magnitude threshold of our data. The curve is the spline fit to this ensemble of mock groups, which is then used to estimate the halo masses as a function of the group richness.

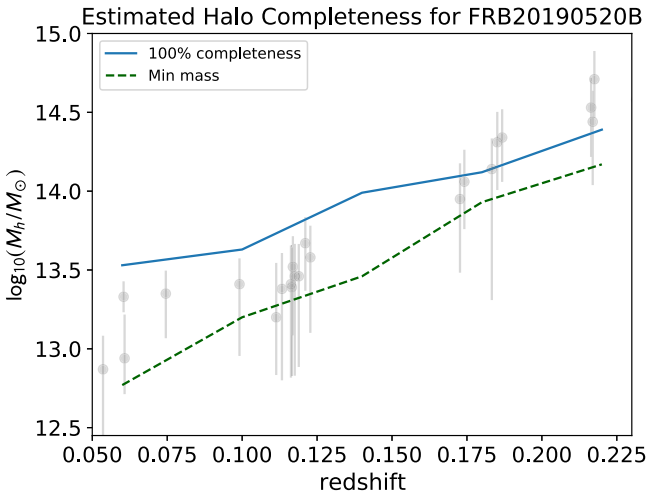

Figure 4. Data points show the redshift and estimated halo masses of the detected groups from our FRB 20190520B spectroscopic data. Curves show the estimated mass completeness of simulated groups and clusters as a function of redshift, assuming the observational depth and completeness of our data. The dashed curve indicates the minimum mass at which groups are detectable with $N_{\rm rich} \geqslant 4$ at the given redshift, while the solid curve indicates the mass at which we expect to be 100% complete.

With the assumption that the free electrons trace the fully ionized circumgalactic halo gas, we use the same halo gas density profile previously adopted in Simha et al. (2020, 2021, 2023), in which the radial profile of the halo baryonic gas density is

$$\rho_b(y) = f_{\rm hot}\left(\frac{\Omega_b}{\Omega_m}\right)\left[\frac{\rho_0(M_{\rm halo})}{y^{1-\alpha}(y_0+y)^{2+\alpha}}\right]. \quad (4)$$

The expression in brackets is a modified Navarro–Frenk–White (NFW; Navarro et al. 1997) radial halo profile for the matter density, as modified by Prochaska & Zheng (2019) in order to approximate the properties of a multiphase circumgalactic medium (CGM; Maller & Bullock 2004). With the central density of ρ_0 set by the halo mass $M_{\rm halo}$, it is a function of y, the scaled radius parameter (see Mathews & Prochaska 2017), while we adopt $\alpha = 2$ and $y_0 = 2$ in this analysis. The ratio $\Omega_b/\Omega_m = 0.157$ is the baryon fraction relative to the overall matter density, while $f_{\rm hot}$ determines the number of baryons that are present in the hot gas of the halo. The truncation radius of the gaseous halo, $r_{\rm max}$, is another free parameter of this model.

In our model, the $\rm DM_{halo}$ contributed by a halo intersected at a fixed impact parameter is therefore a function of $\{M_{\rm halo}, r_{\rm max}, f_{\rm hot}\}$. The uncertainties in $M_{\rm halo}$ have been explicitly estimated in Section 3.1 and will be directly taken into account in the subsequent analysis. To incorporate some of the uncertainties in $r_{\rm max}$ and $f_{\rm hot}$, however, we adopt two different models for the foreground halo contributions that we believe bracket their plausible range.

1. We truncate the gas halos at $r_{\rm max} = r_{200}$. For cluster-sized halos ($M_{\rm halo} > 10^{14}\,M_\odot$), we adopt a halo gas fraction of $f_{\rm hot} = 0.90$. This is driven by X-ray constraints on the baryonic gas fractions in intracluster media that suggest that clusters retain essentially all of their baryonic content thanks to their deep gravitational potentials (e.g., Gonzalez et al. 2013; Chiu et al. 2018). The value of $f_{\rm hot} = 0.90$ assumes that the stars and interstellar medium (ISM) within member galaxies comprise $f_\star \approx 0.1$ of the cluster baryons, with the rest residing in the intracluster medium gas. For lower-mass halos with $M_{\rm halo} < 10^{14}\,M_\odot$, we use the same value of $f_{\rm hot} = 0.75$ that was adopted by Prochaska & Zheng (2019) and Simha et al. (2020), which allows for some of the halo gas to have been expelled from within the characteristic halo radius.
2. The truncation radius of the gas halos is now increased to $r_{\rm max} = 2\,r_{200}$. For cluster halos with $M_{\rm halo} > 10^{14}\,M_\odot$, we again assume $f_{\rm hot} = 0.90$. For the lower-mass halos, however, we introduce a baryonic "cavity" to the central parts of the halos, such that we have $f_{\rm hot} = 0.3$ at $r < r_{200}$ and a "pileup" of evacuated baryons of $f_{\rm hot} = 2$ at $r_{200} < r < 2\,r_{200}$. This is inspired by recent results from hydrodynamical simulations (e.g., Ayromlou et al. 2023; Sorini et al. 2022) that suggest that galaxy or AGN feedback processes can eject baryons from the central regions of galactic halos into the surrounding environment, leaving a reduced baryon fraction in the halo CGM compared with the primordial value.

For brevity, we will refer to the above models as the $r_{\rm max} = r_{200}$ and $r_{\rm max} = 2\,r_{200}$ models, respectively. While it is, in principle, possible for $r_{\rm max}$ to be larger, the modified NFW declines radially, so the $\rm DM_{halo}$ contribution converges with increasing $r_{\rm max}$. For example, for a halo intersected at $b_\perp = 0.5\,r_{200}$, the $\rm DM_{halo}$ increases by 24% when $r_{\rm max}$ is increased from $r_{\rm max} = r_{200}$ to $2\,r_{200}$, but the corresponding increase is only about 5% going from $r_{\rm max} = 2\,r_{200}$ to $3\,r_{200}$.

To compute $\rm DM_{halos}$, we first generate a group halo catalog of the FLIMFLAM spectroscopic data, in which the groups and clusters detected in Section 3 are each treated as individual halos, with the masses estimated from Section 3.1. We then remove the member galaxies of these groups from the overall spectroscopic catalog and treat the remaining field galaxies as individual lower-mass halos.

To assign a halo mass to the field galaxies, we first estimated the stellar masses, $M_\star$, by running the galaxy population

Table 2
Foreground DM_{halo} Contributors

ID	z	R.A.[a] (deg)	Decl.[a] (deg)	$\log_{10}(M_{halo}/M_\odot)$	$b_\perp$ (kpc)	$b_\perp$ (r_{200})	DM_{halo} (pc cm^{-3})[b] $r_{max} = r_{200}$	DM_{halo} (pc cm^{-3})[b] $r_{max} = 2\,r_{200}$
2403390701118753	0.0536	240.3391	−11.1875	$12.87^{+0.21}_{-0.90}$	789	1.58	0^{+20}_{-0}	20^{+65}_{-12}
2405167901131499	0.1862	240.5168	−11.3150	$11.78^{+0.30}_{-0.30}$	313	1.57	0^{+0}_{-0}	10^{+17}_{-10}
2405265701133378	0.1867	240.5266	−11.3338	$14.34^{+0.18}_{-0.28}$	542	0.38	300^{+130}_{-81}	350^{+140}_{-87}
2406051301130845	0.2170	240.6051	−11.3085	$14.44^{+0.20}_{-0.40}$	1156	0.76	110^{+150}_{-50}	180^{+160}_{-52}

Notes.
[a] R.A. and decl. in equatorial J2000 coordinates.
[b] Contribution to the FRB 20190520B DM assuming two different CGM models with $r_{max} = r_{200}$ and 2 r_{200}. We retain only two significant figures of these results.

synthesis code CIGALE (Boquien et al. 2019) on the *griz* photometry, with the redshifts fixed by our spectroscopy. The stellar masses were then converted into halo masses using the stellar mass–halo mass relationship (SHMR) of Moster et al. (2013).

The halo lists from the field galaxies and the identified groups were collated for the DM_{halo} calculation, which integrates the line-of-sight segment through the gas halo profile of Equation (4) assuming the corresponding halo masses, impact parameters from the FRB sight line, and maximum extent of the halo profiles (r_{max}). We did this as a Monte Carlo calculation in order to take into account the uncertainties in the halo masses. For field galaxies, we drew random realizations corresponding to the mean halo mass, as well as a standard deviation of 0.3 dex, the latter of which is a typical halo mass error taking into account uncertainties in the stellar mass estimation, as well as the intrinsic scatter in the SHMR. For the groups and clusters, we sample over the halo mass uncertainties listed in Table 1. However, the χ^2 distributions are asymmetric about the minima; therefore, we approximate this by sampling from an asymmetric Gaussian distribution based on the 16th and 84th percentile errors on either side of the best-fit value. In other words, we first draw the Gaussian random deviate with unit standard deviation and then scale them by the upper or lower error bars depending on whether the draw is positive or negative. We repeat this exercise for ∼100 iterations and keep track of the resulting individual DM_{halo} contributions from every iteration.

In Table 2, we list the foreground halos that provide nonzero contributions to DM_{halos}. The $z_{grp} = 0.1867$ cluster, which is intersected well within its virial radius ($b_\perp \sim 0.4\,r_{200}$), provides the largest contribution, with $DM_{halo} \approx 300$ and 350 pc cm^{-3} assuming the $r_{max} = r_{200}$ and 2 r_{200} models, respectively. There is also a large contribution from the $z_{grp} = 0.2170$ cluster, which has a slightly larger mass but is intersected through its outskirts ($b_\perp \sim 0.8\,r_{200}$). Because of this, the two different truncation radii provide a relatively greater difference for this cluster, changing from $DM_{halo} \approx 110$ to 180 pc cm^{-3} with the increased gas halo radius. The $z_{grp} = 0.1867$ cluster, on the other hand, exhibits a smaller fractional change in DM_{halo} with respect to r_{max}, since the sight line passes through the central region of the halo that gives large contributions with less sensitivity to r_{max}.

There is also a possible contribution from the lower-redshift galaxy group at $z_{grp} = 0.0536$, which has a halo mass of $M_{halo} \approx 9 \times 10^{13}\,M_\odot$ but is intersected at $b_\perp \approx 1.6\,r_{200}$, nominally outside the characteristic halo radius. For the $r_{max} = r_{200}$ model, this clearly cannot contribute to DM_{halos} but does provide a contribution of $DM_{halo} \approx 20$ pc cm^{-3} for the $r_{max} = 2\,r_{200}$ model. In this extended model, another small contribution ($DM_{halo} \approx 10$ pc cm^{-3}) is provided by an individual galaxy at $z = 0.1862$ with a halo mass of $M_{halo} \approx 6 \times 10^{11}\,M_\odot$ also intersected at $b_\perp \approx 1.6\,r_{200}$. While it is debatable whether individual group/cluster members should have their subhalos modeled separately from the main halo, in our case, the difference is negligible.

4.2. IGM Contribution

The FLIMFLAM survey was designed to observe numbers of foreground galaxies to act as tracers for density reconstructions of the large-scale density field in order to enable precise constraints on the DM_{IGM} contribution (e.g., Simha et al. 2020; Lee et al. 2022). However, in the case of FRB 20190520B, the observations were shallower and more incomplete for its FRB redshift due to the significant dust extinction within the field. The FRB 20190520B data were therefore deemed insufficient for density reconstructions using, e.g., methods from Ata et al. (2015), Kitaura et al. (2021), or Horowitz et al. (2019). Therefore, instead of a bespoke calculation of DM_{IGM} based directly on the observed foreground field, in principle, we have to settle for a global estimate of $\langle DM_{IGM}\rangle(z_{frb})$.

However, we do have a catalog of foreground groups and clusters, which we will take into account when trying to estimate $\langle DM_{IGM}\rangle$. Again, we use the "all-sky" Henriques et al. (2015) light-cone catalogs and associated density fields from the Millennium simulation (Springel 2005), largely following the methodology described in Section 3.1 of Lee et al. (2022). In order to avoid double-counting of the group/cluster contributions in both $\langle DM_{IGM}\rangle$ and DM_{halos}, we "clip" the simulation density field within two grid cells of the groups and clusters within the light cone, with the cell values clipped to $\delta \equiv \rho/\langle\rho\rangle - 1 = 3$. Whether or not a group/cluster is clipped from the density field depends on its selection probability as shown in Figure 4, which we implement as a linearly increasing probability with $p = 0$ probability below the minimum detectable halo mass at each redshift to $p = 1$ at masses above the 100% completeness threshold. In other words, for example, at low redshifts ($z < 0.1$), even relatively low-mass groups with $M_{halo} \sim 10^{13}\,M_\odot$ would not be counted in DM_{IGM}, since they can, in principle, be detected in our spectroscopy, and their DM_{halo} contribution is already taken into account. At higher redshifts, such low-mass groups are undetected, and their influence would need to be considered as part of $\langle DM_{IGM}\rangle$. The effect of this halo clipping is to reduce both the mean $\langle DM_{IGM}\rangle$ and its variance.

On the other hand, the FRB 20190520B sight line intersects two separate galaxy clusters, which means that it must be

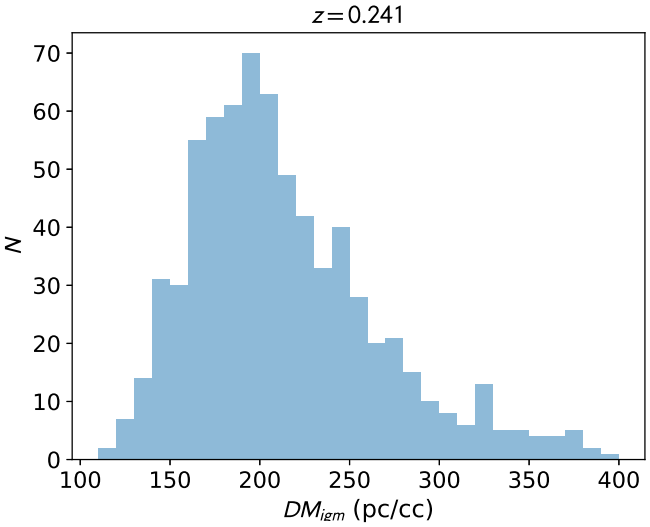

Figure 5. Distribution of $\mathrm{DM_{IGM}}$ for $z_{\rm frb} = 0.241$ sight lines in the Millennium simulation box, selected to intersect two $M_{\rm halo} > 10^{14}\,M_{\odot}$ halos. The direct influence of groups and halos has been removed according to the selection function of Figure 4. We assume $f_{\rm igm} = 0.85$ for this calculation.

crossing through overdense regions of the Universe even if we have already removed the direct influence of the clusters themselves within ∼1–2 Mpc. For the $\langle \mathrm{DM_{IGM}} \rangle$ calculation, we therefore selected mock sight lines at $z_{\rm frb} = 0.241 \pm 0.001$ that intersect within r_{200} of two clusters with $M_{\rm halo} > 10^{14}\,M_{\odot}$. Compared with randomly selected sight lines at this redshift selected to originate within galaxies with an observed magnitude of $r < 20$ (see, e.g., Pol et al. 2019), we find that 0.07% of the sight lines intersect two separate foreground cluster halos, i.e., ∼1 in 1400.

We integrate the selected sight lines through Millennium density fields that have already been clipped of "observed" clusters and compute $\mathrm{DM_{IGM}}$ assuming $f_{\rm igm} = 0.85$, which is the typical fraction of cosmic baryons expected to reside in the diffuse IGM as found in cosmological hydrodynamical simulations (e.g., Jaroszynski 2019; Batten et al. 2021; Takahashi et al. 2021; Zhang et al. 2021; Zhu & Feng 2021). The resulting $\mathrm{DM_{IGM}}$ distribution is shown in Figure 5 with a median $\langle \mathrm{DM_{IGM}} \rangle (z = 0.241) = 204^{+62}_{-39}$ pc cm^{-3}, where the errors are quoted at the 16th and 84th percentiles. In comparison, for random sight lines at the same redshift through the normal "unclipped" density field, we find $\langle \mathrm{DM_{IGM}} \rangle = 191^{+64}_{-39}$ pc cm^{-3}, while for random sight lines through the clipped density fields, we get $\langle \mathrm{DM_{IGM}} \rangle = 179^{+51}_{-33}$. The effects of clipping the influence of group/cluster halos and selecting sight lines that go through two clusters thus appear to largely cancel each other out, although the median $\mathrm{DM_{IGM}}$ for our double-cluster sight lines is indeed slightly higher than the usual mean.

4.3. The Host DM of FRB 20190520B

With the estimates of the foreground contributions in hand, we now subtract these from the total DM of FRB 20190520B in order to constrain the host contribution. Since the distributions for $\mathrm{DM_{IGM}}$ and $\mathrm{DM_{halos}}$ are significantly non-Gaussian, instead of propagating errors, we take the direct route of calculating the distribution of $\mathrm{DM_{host}}$ based on the Monte Carlo realizations we have calculated for $\mathrm{DM_{IGM}}$ and $\mathrm{DM_{halos}}$.

Table 3
FRB 20190520B DM Components

Component[a]	$r_{\rm max} = r_{200}$	$r_{\rm max} = 2\,r_{200}$
$\mathrm{DM_{FRB}}$	1205^{+4}_{-4}	
$\mathrm{DM_{MW}}$	113^{+13}_{-13}	
$\mathrm{DM_{IGM}}$	204^{+62}_{-39}	
$\mathrm{DM_{halos}}$	450^{+240}_{-130}	640^{+260}_{-150}
$\mathrm{DM_{host}}$[b]	430^{+140}_{-220}	280^{+140}_{-170}

Notes.
[a] All DM values are in units of pc cm^{-3}.
[b] In the observed frame.

In other words, we compute multiple iterations of

$$\mathrm{DM_{host,}}_i = \mathrm{DM_{FRB,}}_i - \mathrm{DM_{MW,}}_i - \mathrm{DM_{IGM,}}_i - \mathrm{DM_{halos,}}_i, \quad (5)$$

where $\mathrm{DM_{halos,}}_i$ and $\mathrm{DM_{IGM,}}_i$ were drawn from the Monte Carlo realizations computed in Sections 4.1 and 4.2, respectively. For $\mathrm{DM_{FRB,}}_i$ and $\mathrm{DM_{MW,}}_i$, we draw Gaussian random deviates for each iteration based on the values reported by Niu et al. (2022), $\mathrm{DM_{FRB}} = (1205 \pm 4)$ and $\mathrm{DM_{MW}} = (113 \pm 17)$ pc cm^{-3}, where the uncertainties are adopted as the Gaussian standard deviations. We enforce the prior that $\mathrm{DM_{host}} \geqslant 0$ pc cm^{-3}.

After computing Equation (5) over $N = 2000$ iterations, we compute the median and 16th/84th percentiles of the resulting $\mathrm{DM_{host,}}_i$ distribution. These quantities, as well as the individual DM components, are listed in Table 3; note that since the medians are listed for each component, they do not necessarily obey Equation (3) precisely.

We separately calculated the $\mathrm{DM_{host}}$ for the two different assumptions of $r_{\rm max}$ for the foreground halo contributions. Assuming $r_{\rm max} = r_{200}$ (see Section 4.1), we find $\mathrm{DM_{host}} = 430^{+140}_{-220}$ pc cm^{-3}; on the other hand, for the $r_{\rm max} = 2\,r_{200}$ model, the resulting host contribution is $\mathrm{DM_{host}} = 280^{+140}_{-170}$ pc cm^{-3} (both in the observed frame; the corresponding rest-frame values are $\mathrm{DM_{host}} = 540^{+170}_{-270}$ and 350^{+180}_{-210} pc cm^{-3}, respectively). These estimates are much lower than the value of $\mathrm{DM_{host}} = 903^{+72}_{-111}$ pc cm^{-3} originally reported by Niu et al. (2022). The 68th percentile errors we derive are significantly larger than the Niu et al. (2022) estimate, since they are driven by the uncertainties in the foreground cluster masses. Adopting the upper 68th percentile errors of our $\mathrm{DM_{host}}$ values as a σ, the original estimate for $\mathrm{DM_{host}}$ is 3.4σ and 4.3σ away from our $r_{\rm max} = r_{200}$ and $2\,r_{200}$ model estimates, respectively.

5. Discussion

The $\mathrm{DM_{host}}$ of FRBs arise from all the free electron contributions in the host galaxy and the immediate vicinity of the FRB, starting from the so-far mysterious source engine, ionized ISM gas, and then CGM of the host galaxy.[17] For localized FRBs with a clearly identified host galaxy, it is, in principle, straightforward to calculate the halo mass and estimate the halo CGM contribution $\mathrm{DM_{host}^{cgm}}$ the same way

[17] If the FRB host galaxy is embedded in a galaxy cluster or group, then the cluster contribution is typically considered separately; see, e.g., Connor et al. (2023).

we did for the foreground halos, so we can write

$$\mathrm{DM_{host}} = \mathrm{DM_{host}^{cgm}} + \mathrm{DM_{host}^{in}}, \quad (6)$$

where we define $\mathrm{DM_{host}^{in}}$ as the "inner" DM components arising from the source engine and galaxy stellar/ISM component.

5.1. Host Halo Contribution

Given the association of FRB 20190520B with the $z = 0.241$ host galaxy HG 20190520B by Niu et al. (2022), we can start by estimating the contribution from the CGM of the host halo. For the reported stellar mass of $M_\star \approx 6 \times 10^8\, M_\odot$ (Niu et al. 2022), we use the dwarf galaxy SHMR of Read et al. (2017) to estimate a halo mass of $M_{\rm halo} = 9 \times 10^{10}\, M_\odot$. Allowing for the fact that the FRB originates 5 kpc (Niu et al. 2022) from the galaxy center, and adopting the models described in Section 4.1, we estimate rest-frame CGM contributions of $\mathrm{DM_{host}^{cgm}} = 18$ and 12 pc cm^{-3} assuming the $r_{\rm max} = r_{200}$ and $2\, r_{200}$ models, respectively. In other words, the CGM of HG 20190520B provides only a small contribution to the $\mathrm{DM_{host}}$ of FRB 20190520B. This allows us to estimate the rest-frame values of the inner host contribution to be $\mathrm{DM_{host}^{in}} \approx 520^{+170}_{-270}$ and 330^{+180}_{-210}, where we have neglected the error on $\mathrm{DM_{host}^{cgm}}$ due to the small central value.

5.2. Emission Measures and Scattering

In their analysis of FRB 20190520B, Niu et al. (2022) and Ocker et al. (2022) evaluated the emission measure (EM) from the observed optical Hα lines in HG 20190520B, which can be converted into an equivalent DM (Tendulkar et al. 2017). This was found to yield an observed-frame value in the range $\mathrm{DM_{host}} \approx 230$–$650$ pc cm^{-3}, which was in tension with the original estimate of $\mathrm{DM_{host}} = 903$ pc cm^{-3}. In comparison, our new estimate for the inner host contribution spans a 68th percentile confidence region of approximately $\mathrm{DM_{host}} \sim 110$–$690$ pc cm^{-3} (after combining results from both models in Section 4.1). The EM estimation is thus now in agreement with $\mathrm{DM_{host}}$ without having to invoke unusually high gas temperatures ($T \gg 10^4$ K) in the Hα-emitting medium, as suggested by Ocker et al. (2022). Given the broad agreement between the EM and DM estimates, the Hα emitting gas—presumably in the galaxy disk—also now appears to make up the bulk of the ionized medium responsible for the dispersion seen in HG 20190520B.

Across a large number of repeating signals, FRB 20190520B has also been measured by Ocker et al. (2022) to have a mean scattering time delay of $\tau = 10.9 \pm 1.5$ ms (measured at 1.41 GHz) that can be attributed to the host. This DM of the scattering screen can be estimated from the scattering timescale using the expression from Cordes et al. (2022),

$$\tau(\mathrm{DM}, \nu, z) \approx 48.03\ \mu s\ \times \frac{A_\tau \widetilde{F} G \mathrm{DM}^2}{(1 + z_{\rm frb})^3\, \nu^4}, \quad (7)$$

where ν is the measured frequency in gigahertz. The A_τ is a dimensionless quantity relating the mean scattering delay to the $1/e$ time, which we assume to be $A_\tau \approx 1$ following Ocker et al. (2022). The combined factor $\widetilde{F}G$ describes the combined amplification from turbulent density fluctuations and the geometry of the scattering screen, respectively, which Ocker et al. (2022) estimated to be $\widetilde{F}G = 1.5^{+0.8}_{-0.3}$(pc^2 km)$^{-1/3}$ using the old value of $\mathrm{DM_{host}} = 903$ pc cm^{-3}.

With our updated rest-frame $\mathrm{DM_{host}^{in}}$ values for FRB 20190520B (Section 5.1), we recalculate $\widetilde{F}G \propto 1/\mathrm{DM}^2$ to find $\widetilde{F}G \approx 4.5$–$11$ (pc^2 km)$^{-1/3}$, with the range allowing for our model uncertainty in subtracting off the foreground galaxy clusters. This contrasts with the value originally estimated by Ocker et al. (2022), which is close to unity. This larger value implies that either $\widetilde{F} > 1$, $G > 1$, or both. If $\widetilde{F} > 1$, it would imply that the scattering screen is highly turbulent. Meanwhile, $G \approx 1$ is expected if the turbulent scattering screen is close to the source, but it could be greater than unity if the screen is somewhere along the intervening path yet still farther away from the Milky Way, e.g., if they were associated with the foreground clusters. However, Connor et al. (2023) recently studied two FRBs that were localized to host galaxies embedded within galaxy clusters and did not see significant scattering in those FRB signals. We therefore consider it unlikely that foreground clusters are the source of the scattering; it is more likely that the large $\widetilde{F}G$ value is due to a highly turbulent scattering screen associated with the host and perhaps even close to the FRB engine itself. This conclusion is corroborated by the recent Ocker et al. (2023) paper, which reports significant scattering variations in the repeated FRB 20190520B signals, as well as the sign changes observed in their Faraday rotation (Anna-Thomas et al. 2023).

5.3. FRB 20190520B in Context

When FRB 20190520B was discovered, its $\mathrm{DM_{host}}$ estimate and those of nearly all other localized FRBs were done through guesstimated $\mathrm{DM_{host}}$ values after subtracting the mean $\langle \mathrm{DM_{IGM}} \rangle(z)$. At the time of writing, approximately a half-dozen localized FRBs now have credible foreground analyses that enable more confidence in their estimated $\mathrm{DM_{host}}$.

Arguably the first reliable estimate was done by Simha et al. (2020), who analyzed the foreground of FRB 20190608 based on Sloan Digital Sky Survey and Keck data using an analogous technique to ours. They estimated $\mathrm{DM_{host}} \approx 80$–$200$ pc cm^{-3} (observed frame), which is in fact consistent with an independent analysis of the host galaxy (Chittidi et al. 2021).

More recently, Simha et al. (2023) analyzed four FRB sight lines known to exhibit DMs significantly higher than the cosmic mean using FLIMFLAM spectroscopic data of the foreground fields.

Like FRB 20190520B, FRB 20210117A was suspected to be a high-$\mathrm{DM_{host}}$ source given its clear excess $\mathrm{DM_{FRB}} = 731$ pc cm^{-3} and localized redshift of $z_{\rm frb} = 0.2145$. However, unlike FRB 20190520B, no significant excess was found from $\mathrm{DM_{halos}}$ based on the foreground data, so it is confirmed to be a high-$\mathrm{DM_{host}}$ source, with $\mathrm{DM_{host}} \approx 665$ pc cm^{-3} in the rest frame. This is in fact higher than the revised rest-frame values of $\mathrm{DM_{host}} \sim 350$–$540$ pc cm^{-3} we now find for FRB 20190520B, which now makes FRB 20210117A in principle the FRB with the highest known $\mathrm{DM_{host}}$, although the uncertainties are large enough for either to be the true record holder. Also, FRB 20200906A was shown to not have significant foreground contributions despite a high $\mathrm{DM_{FRB}}$, yielding an estimate of $\mathrm{DM_{host}} \approx 420$ pc cm^{-3}. Both FRB 20190714A and FRB 20200430A are shown to have significant foreground contributions; thus, they do not have large $\mathrm{DM_{host}}$. We note that this subsample is explicitly biased toward excess DM sources; thus, it is possible that the $\mathrm{DM_{host}}$ from this sample might be biased high as well, even though some of the FRBs are shown to be from overdense foregrounds.

James et al. (2022) and, subsequently, Baptista et al. (2023) performed population modeling of a sample of ≈70 FRBs, including 21 with redshifts from host associations. Their forward model includes two parameters to describe a lognormal distribution for $\mathrm{DM_{host}}$. Taking their preferred values of $\sigma = 0.5$ and $\mu = 2.43$, we find that 40% of the FRB hosts are expected to have $\mathrm{DM_{host}} > 500\,\mathrm{pc\,cm^{-3}}$. We conclude, therefore, that our inferred value for FRB 20190520B is consistent with the full population.

6. Conclusion

In this paper, we used wide-field spectroscopic data from the FLIMFLAM survey targeting the field of FRB 20190520B to study the possible foreground contributions to the overall observed DM, which is anomalously high ($\mathrm{DM_{FRB}} = 1205\,\mathrm{pc\,cm^{-3}}$) given its confirmed redshift. Our data show that the FRB 20190520B sight line directly intersects two foreground galaxy clusters at $z = 0.1867$ and 0.2170 within their virial radii in a rare occurrence estimated to happen to only ∼1 in 1400 sight lines at this FRB path length. These two foreground clusters yield a combined contribution of $\mathrm{DM_{halos}} \sim 450$–$640\,\mathrm{pc\,cm^{-3}}$, which allows us to revise the host contribution downward to $\mathrm{DM_{host}} \sim 280$–$430\,\mathrm{pc\,cm^{-3}}$ after also taking into account the Milky Way and diffuse IGM contributions (see Table 3 for detailed values). This means that FRB 20190520B is no longer the FRB with the largest host DM contribution, with FRB 20210117A now being the source with the largest known $\mathrm{DM_{host}}$, but they are similar to within the uncertainties. The new value for $\mathrm{DM_{host}}$ is now in agreement with Hα emission estimates of $\mathrm{DM_{host}}$ and allowed us to make a revised estimate of the combined factor describing geometric effects and turbulent density fluctuations based on the scattering timescale: $\widetilde{F}G \approx 4.5$–$11\ (\mathrm{pc^2\,km})^{-1/3}$. We interpret this as due to high turbulence in the scattering screen associated with the host, since we consider it unlikely that the foreground halos are the source of the scattering.

This result outlines the importance of obtaining sufficiently wide-field foreground spectroscopy in disentangling the various DM contributions in FRBs, both for their usage as cosmological probes and for understanding their host progenitors. The original Keck/LRIS optical spectroscopy from Niu et al. (2022) consisted of single-slit observations, but even if they had utilized multiobject slit masks to target some of the foreground galaxies, they would have been limited to within 2′–3′ of the FRB position by the limited field of view of LRIS (see the interactive version of Figure 2). The LRIS observations might have captured two to three of the $z_{\mathrm{grp}} = 0.1867$ group members, but the rest lie 4′–5′ away from the FRB. The member galaxies of the $z_{\mathrm{grp}} = 0.2170$ group, on the other hand, lie mostly ∼5′–6′ away from FRB 20190520B and would likely have been missed even with multiobject spectroscopy with LRIS or equivalent narrow-field spectrographs on other telescopes.

Our present result on FRB 20190520B is a vivid illustration of the power of foreground data in enhancing the use of FRBs. In Lee et al. (2022), we estimated that wide-field foreground spectroscopy enhances the power of localized FRBs as cosmological probes by a factor of ∼30 in terms of the number of FRBs required to achieve comparable constraints, whereas in comparison with unlocalized FRBs, this is an enhancement by factors of $\sim 10^2$–10^3 (Shirasaki et al. 2022; Wu & McQuinn 2023).

In an upcoming paper (I. Khrykin et al. 2023, in preparation), we will present the first cosmic baryon analysis from a preliminary sample of FLIMFLAM fields that will give the first constraints on the partition of cosmic baryons between the IGM and CGM.

Acknowledgments

We are grateful to Elmo Tempel for kindly sharing his group-finding code, Chris Lidman for helping with the data reduction code, and various members of the CRAFT collaboration for useful discussions. K.N. acknowledges support from MEXT/JSPS KAKENHI grants JP17H01111, 19H05810, and 20H00180, as well as travel support from Kavli IPMU, World Premier Research Center Initiative, where part of this work was conducted. We acknowledge generous financial support from Kavli IPMU that made FLIMFLAM possible. Kavli IPMU is supported by the World Premier International Research Center Initiative (WPI), MEXT, Japan. Based on data acquired at the Anglo-Australian Telescope under programs A/2020B/04, A/2021A/13, and O/2021A/3001. We acknowledge the traditional custodians of the land on which the AAT stands, the Gamilaraay people, and pay our respects to elders past and present. S.S., J.X.P., I.K., and N.T., as members of the Fast and Fortunate for FRB Follow-up team, acknowledge support from NSF grants AST-1911140, AST-1910471, and AST-2206490.

Software: configure (Miszalski et al. 2006), MARZ (Hinton et al. 2016), CIGALE (Boquien et al. 2019), Astropy (Astropy Collaboration et al. 2022), Numpy (Harris et al. 2020), Scipy (Virtanen et al. 2020), Matplotlib (Hunter 2007), Bokeh.

ORCID iDs

Khee-Gan Lee https://orcid.org/0000-0001-9299-5719
Ilya S. Khrykin https://orcid.org/0000-0003-0574-7421
Sunil Simha https://orcid.org/0000-0003-3801-1496
Metin Ata https://orcid.org/0000-0002-5934-9018
Yuxin Huang https://orcid.org/0000-0002-0298-8898
J. Xavier Prochaska https://orcid.org/0000-0002-7738-6875
Nicolas Tejos https://orcid.org/0000-0002-1883-4252
Jeff Cooke https://orcid.org/0000-0001-5703-2108
Kentaro Nagamine https://orcid.org/0000-0001-7457-8487
Jielai Zhang https://orcid.org/0000-0001-5310-4186

References

Anna-Thomas, R., Connor, L., Dai, S., et al. 2023, Sci, 380, 599
Astropy Collaboration, Price-Whelan, A. M., & Lim, P. L. 2022, ApJ, 935, 167
Ata, M., Kitaura, F.-S., & Müller, V. 2015, MNRAS, 446, 4250
Ayromlou, M., Nelson, D., & Pillepich, A. 2023, MNRAS, 524, 5391
Baptista, J., Prochaska, J. X., Mannings, A. G., et al. 2023, arXiv:2305.07022
Batten, A. J., Duffy, A. R., Wijers, N. A., et al. 2021, MNRAS, 505, 5356
Bertin, E., & Arnouts, S. 1996, A&AS, 117, 393
Boquien, M., Burgarella, D., Roehlly, Y., et al. 2019, A&A, 622, A103
Childress, M. J., Lidman, C., Davis, T. M., et al. 2017, MNRAS, 472, 273
Chittidi, J. S., Simha, S., Mannings, A., et al. 2021, ApJ, 922, 173
Chiu, I., Mohr, J. J., McDonald, M., et al. 2018, MNRAS, 478, 3072
Connor, L., Ravi, V., Catha, M., et al. 2023, ApJL, 949, L26
Cook, A. M., Bhardwaj, M., Gaensler, B. M., et al. 2023, ApJ, 946, 58
Cordes, J. M., & Lazio, T. J. W. 2002, arXiv:astro-ph/0207156
Cordes, J. M., Ocker, S. K., & Chatterjee, S. 2022, ApJ, 931, 88
Gonzalez, A. H., Sivanandam, S., Zabludoff, A. I., & Zaritsky, D. 2013, ApJ, 778, 14
Guo, Q., White, S., Boylan-Kolchin, M., et al. 2011, MNRAS, 413, 101
Harris, C. R., Millman, K. J., van der Walt, S. J., et al. 2020, Natur, 585, 357

Henriques, B. M. B., White, S. D. M., Thomas, P. A., et al. 2015, MNRAS, 451, 2663
Hinton, S. R., Davis, T. M., Lidman, C., Glazebrook, K., & Lewis, G. F. 2016, A&C, 15, 61
Horowitz, B., Lee, K.-G., White, M., Krolewski, A., & Ata, M. 2019, ApJ, 887, 61
Hunter, J. D. 2007, CSE, 9, 90
Inoue, S. 2004, MNRAS, 348, 999
Ioka, K. 2003, ApJL, 598, L79
James, C. W., Ghosh, E. M., Prochaska, J. X., et al. 2022, MNRAS, 516, 4862
Jaroszynski, M. 2019, MNRAS, 484, 1637
Kitaura, F.-S., Ata, M., Rodríguez-Torres, S. A., et al. 2021, MNRAS, 502, 3456
Law, C. J., Bower, G. C., Burke-Spolaor, S., et al. 2018, ApJS, 236, 8
Lee, K.-G., Ata, M., Khrykin, I. S., et al. 2022, ApJ, 928, 9
Li, D., Wang, P., Qian, L., et al. 2018, IMMag, 19, 112
Macquart, J. P., Prochaska, J. X., McQuinn, M., et al. 2020, Natur, 581, 391
Maller, A. H., & Bullock, J. S. 2004, MNRAS, 355, 694
Mathews, W. G., & Prochaska, J. X. 2017, ApJL, 846, L24
Miszalski, B., Shortridge, K., Saunders, W., Parker, Q. A., & Croom, S. M. 2006, MNRAS, 371, 1537
Moster, B. P., Naab, T., & White, S. D. M. 2013, MNRAS, 428, 3121
Nan, R., Li, D., Jin, C., et al. 2011, IJMPD, 20, 989
Navarro, J. F., Frenk, C. S., & White, S. D. M. 1997, ApJ, 490, 493
Niu, C. H., Aggarwal, K., Li, D., et al. 2022, Natur, 606, 873
Ocker, S. K., Cordes, J. M., Chatterjee, S., et al. 2022, ApJ, 931, 87
Ocker, S. K., Cordes, J. M., Chatterjee, S., et al. 2023, MNRAS, 519, 821
Pol, N., Lam, M. T., McLaughlin, M. A., Lazio, T. J. W., & Cordes, J. M. 2019, ApJ, 886, 135
Prochaska, J. X., & Zheng, Y. 2019, MNRAS, 485, 648
Ravi, V., Catha, M., Chen, G., et al. 2023, arXiv:2301.01000
Read, J. I., Iorio, G., Agertz, O., & Fraternali, F. 2017, MNRAS, 467, 2019
Schlafly, E. F., & Finkbeiner, D. P. 2011, ApJ, 737, 103
Shirasaki, M., Takahashi, R., Osato, K., & Ioka, K. 2022, MNRAS, 512, 1730
Simha, S., Burchett, J. N., Prochaska, J. X., et al. 2020, ApJ, 901, 134
Simha, S., Lee, K.-G., Prochaska, J. X., et al. 2023, arXiv:2303.07387
Simha, S., Tejos, N., Prochaska, J. X., et al. 2021, ApJ, 921, 134
Sorini, D., Davé, R., Cui, W., & Appleby, S. 2022, MNRAS, 516, 883
Springel, V. 2005, MNRAS, 364, 1105
Tago, E., Einasto, J., Saar, E., et al. 2008, A&A, 479, 927
Takahashi, R., Ioka, K., Mori, A., & Funahashi, K. 2021, MNRAS, 502, 2615
Tempel, E., Tago, E., & Liivamägi, L. J. 2012, A&A, 540, A106
Tempel, E., Tamm, A., Gramann, M., et al. 2014, A&A, 566, A1
Tendulkar, S. P., Bassa, C. G., Cordes, J. M., et al. 2017, ApJL, 834, L7
Virtanen, P., Gommers, R., Oliphant, T. E., et al. 2020, NatMe, 17, 261
Wu, X., & McQuinn, M. 2023, ApJ, 945, 87
Yao, J. M., Manchester, R. N., & Wang, N. 2017, ApJ, 835, 29
Yuan, F., Lidman, C., Davis, T. M., et al. 2015, MNRAS, 452, 3047
Zhang, Z. J., Yan, K., Li, C. M., Zhang, G. Q., & Wang, F. Y. 2021, ApJ, 906, 49
Zhu, W., & Feng, L.-L. 2021, ApJ, 906, 95